crystals

MDPI

Article

DFT Investigation into Adsorption–Desorption Properties of Mg/Ni-Doped Calcium-Based Materials

Wei Shi [1], Renwei Li [2], Xin Bao [3], Haifeng Yang [4] and Dehao Kong [1,*]

[1] School of New Energy and Materials, Northeast Petroleum University, Daqing 163711, China
[2] College of Mechanical and Electrical Engineering, Jilin Institute of Chemical Technology, Jilin 132022, China
[3] Key Laboratory of Functional Materials Physics and Chemistry of the Ministry of Education, Jilin Normal University, Changchun 130103, China
[4] State Key Laboratory of Advanced Welding and Joining, Harbin Institute of Technology, Weihai 264209, China
* Correspondence: kongdehao1997@163.com

Abstract

Although concentrated solar power (CSP) coupled with calcium looping (CaL) offers a promising avenue for efficient thermal chemical energy storage, calcium-based sorbents suffer from accelerated structural degradation and decreased CO_2 capture capacity during multiple cycles. This study used Density Functional Theory (DFT) calculations to investigate the mechanism by which Mg and Ni doping improves the adsorption/desorption performance of CaO. The DFT results indicate that Mg and Ni doping can effectively reduce the formation energy of oxygen vacancies on the CaO surface. Mg–Ni co-doping exhibits a significant synergistic effect, with the formation energy of oxygen vacancies reduced to 5.072 eV. Meanwhile, the O^{2-} diffusion energy barrier in the co-doped system was reduced to 2.692 eV, significantly improving the ion transport efficiency. In terms of CO_2 adsorption, Mg and Ni co-doping enhances the interaction between surface O atoms and CO_2, increasing the adsorption energy to −1.703 eV and forming a more stable CO_3^{2-} structure. For the desorption process, Mg and Ni co-doping restructured the $CaCO_3$ surface structure, reducing the CO_2 desorption energy barrier to 3.922 eV and significantly promoting carbonate decomposition. This work reveals, at the molecular level, how Mg and Ni doping optimizes adsorption–desorption in calcium-based materials, providing theoretical guidance for designing high-performance sorbents.

Keywords: thermochemical energy storage; concentrated solar power; adsorption–desorption properties; synergistic effect; density functional theory

check for updates

Academic Editor: Thomas M. Klapötke

Received: 6 July 2025
Revised: 30 July 2025
Accepted: 1 August 2025
Published: 3 August 2025

Citation: Shi, W.; Li, R.; Bao, X.; Yang, H.; Kong, D. DFT Investigation into Adsorption–Desorption Properties of Mg/Ni-Doped Calcium-Based Materials. *Crystals* **2025**, *15*, 711. https://doi.org/10.3390/cryst15080711

Copyright: © 2025 by the authors. Licensee MDPI, Basel, Switzerland. This article is an open access article distributed under the terms and conditions of the Creative Commons Attribution (CC BY) license (https://creativecommons.org/licenses/by/4.0/).

1. Introduction

In the context of accelerated global energy transition, solar energy—a core component of clean energy—faces challenges in its practical applications due to its intermittent and fluctuating nature, requiring urgent breakthroughs [1,2]. Coupling concentrated solar power (CSP) with calcium looping (CaL) technology is a promising approach to building stable and efficient solar power generation systems [3–5]. The synergy between CSP and CaL presents the following advantages: (a) High-temperature operating characteristics support efficient vapor cycling, which significantly improves overall thermal efficiency [5]. (b) The energy storage density is extremely high, reaching up to 3.2 GJ/m^3 [6]. (c) The

solidification is not a concern for the reactants and products during room-temperature storage [7]. The key chemical reaction governing the CaL process is

$$CaCO_3 \rightarrow CaO + CO_2 \quad (1)$$

$$CaO + CO_2 \rightarrow CaCO_3 \quad (2)$$

During periods of sufficient sunlight, high-temperature heat drives the calcination of $CaCO_3$. This process converts solar energy into chemical energy stored within the resulting CaO and CO_2. When solar radiation is inadequate, the stored CaO reacts with CO_2 through carbonation, releasing heat to sustain power generation for continuous operation. During CSP–CaL operation, calcium-based materials experience severe structural degradation under high-temperature (800–900 °C) carbonation in concentrated CO_2 atmospheres. This manifests as a substantial reduction in specific surface area, progressive pore collapse, and declining porosity. Concurrently, the rapid formation of a dense $CaCO_3$ product layer on particle surfaces creates a diffusion barrier, impeding CO_2 transport to the unreacted core. These degradation mechanisms intensify cyclically, leading to a significant decline in the material's effective conversion rate over repeated carbonation–calcination cycles [8–10].

Various solutions have been successively proposed, such as acoustic perturbation-based approaches [11], mechanical activation processes [12,13], multi-shelled structures [14], steam activation processes [15,16], thermally activated treatment techniques [17–19], and reaction pressure regulation strategies [20,21]. Notably, material doping is an important research direction for enhancing the performance of calcium-based sorbents. At present, the doping systems are broadly categorized into two categories. The first is alkali metal salt promoters. They expedite the formation of carbonate ions by boosting the transport efficiency of oxide ions. Meanwhile, the high-temperature treatment time is shortened to avoid structural sintering triggered by exceeding the Taman temperature. Referring to the research by Huang et al. [22], their experiments used alkali metal carbonates as activators and successfully prepared a series of CaO-based sorbents. Performance tests revealed that, compared to pure CaO, the sorbents activated with alkali metal carbonates exhibited significant advantages in adsorption performance. In the single-salt activation system, the activation effects of different alkali metal carbonates showed obvious differences, with K_2CO_3 being the most effective. Further investigation of multi-salt systems has confirmed that binary and ternary salt combinations have a better activating effect than single salts, demonstrating performance improvements resulting from synergistic activation effects. Meanwhile, CO_2 absorption can only be promoted when the adsorption temperature is higher than the melting point of the molten salt coated on the particles. This is because the alkali metal carbonate coating prevents the formation of a hard $CaCO_3$ layer on the CaO surface and provides continuous transport of CO_3^{2-} to facilitate CO_2 capture. When $CaCO_3$ accumulates to saturation in the molten salt, a permeable $CaCO_3$ layer is formed so that the reaction is not limited by diffusion. The molten salt penetrates this layer to dissolve CaO, thereby increasing CO_2 adsorption. According to the research of Xu et al. [23], K_2CO_3-doped CaO sorbents were successfully prepared by the hydration impregnation method. The experimental data indicated that under mild and severe CO_2 conditions, low K_2CO_3 doping could significantly improve the cycle stability of CaO sorbents. However, as the K_2CO_3 doping content increases, the enhancement effect on CO_2 adsorption performance shows a decreasing trend. Further investigation into the mechanism reveals that in a CO_2 atmosphere, CaO and K_2CO_3 readily undergo solid-state reactions, first forming the intermediate product $K_2Ca(CO_3)_2$, which further participates in the reaction to generate $K_2Ca_2(CO_3)_3$. The formation of these double salt products alters the structural evolution pathway of the $CaCO_3$ phase during the carbonation reaction, leading to changes in the pore

structure and distribution of active sites of the sorbent, ultimately resulting in differences in adsorption performance at different doping levels. According to the research by Cui et al. [24], LiCl, NaCl, KCl, and $CaCl_2$ were successfully incorporated into the CaO matrix using the hydration impregnation method. Systematic research found that the carbonization reaction mode of CaO sorbents is closely related to the melting point of the added alkali metal chloride salts. When the temperature reaches the melting point of the chloride salts, the molten chloride salts dissolve the CaO to form unique ion diffusion channels, which significantly increase the migration rate of free CaO ions, thereby effectively accelerating the carbonization reaction process. Cycling performance test results show that after 20 cycles, the optimal doped sorbent exhibits a 214% improvement in energy storage performance compared to pure CaO, demonstrating excellent application potential. Gonzalez et al. [25] investigated the effect of KCl doping on the performance of CaO-based sorbents using the hydration impregnation method. The results indicated that a small amount of KCl doping could enhance the CO_2 adsorption performance of CaO-based sorbents, and this enhancement originated from the fact that K^+ in the sorbent could increase the mobility of ions. Yuan et al. [26] prepared binary sulfate and Al-Mn-Fe oxide co-doped CaO-based sorbents by the sol–gel method. Performance test data shows that the energy storage density of this sorbent reaches 1455 kJ/kg. After 100 cycles, its performance degradation rate is only 4.91%, demonstrating excellent stability. In addition, the peak decomposition rate of the sorbent was increased by 120% compared to $CaCO_3$. This significant improvement can be attributed to the lower activation energy of binary sulfate, which can effectively reduce the energy barrier required for the reaction. Meanwhile, the promotion of Ca^{2+} diffusion by binary sulfate accelerates the ion migration rate, thereby significantly improving the decomposition efficiency of the sorbent. At high temperatures, the carbonization rate of the sorbent increased by 10% compared to $CaCO_3$, which stems from the excellent oxygen transport capacity of the binary sulfate.

In our prior research, we discovered that doping CaO with Na_2SO_4, NaCl, KCl, or a combination of Na_2SO_4 and NaCl can enhance its adsorption rate. However, the presence of Na^+ exacerbates material surface densification, ultimately resulting in performance decline [27–29]. In the practical application of CaL technology, maintaining the long-term cycling stability of sorbents has always been a key challenge that needs to be overcome. Against this backdrop, inert oxides have gradually become the focus of the research. These inert oxides, which have excellent thermal stability, can be dispersed in a highly uniform state within the CaO matrix. They effectively inhibit high-temperature migration at the CaO grain boundaries and significantly reduce grain coarsening. To date, macroscopic experimental research has achieved considerable progress, yet in-depth theoretical analysis at the molecular level is still required.

In this work, DFT calculations were systematically used to investigate the enhancement mechanisms of the adsorption and desorption properties of calcium-based materials by Mg doping, Ni doping, and Mg–Ni co-doping. This work aims to reveal the microscopic interaction mechanisms between Mg and Ni atoms and the $CaO/CaCO_3$ surface at the molecular level. Through energy calculations, changes in CO_2 adsorption/desorption behavior and electronic structure evolution have been revealed, paving the way for the development and application of high-performance calcium-based sorbents.

2. Simulation Details

Based on the first-principles calculation framework, a high-precision atomic model was constructed using the CASTEP calculation module embedded with Density Functional Theory (DFT) [30]. The Perdew–Burke–Ernzerhof (PBE) exchange-correlation functional under the Generalized Gradient Approximation (GGA) is utilized in the computational

procedure. To ensure the convergence of integrals in the Brillouin zone, the cut-off energy is set at 720 eV, and the k-points are configured as 2 × 2 × 2 [31–33]. To ensure the reliability and accuracy of the computational structure, this study established stringent convergence criteria during the system optimization process. Specifically, the energy convergence threshold was set to less than 10^{-5} eV to ensure that the system energy reached a stable state. The maximum allowable value of interatomic interaction force was set to 0.03 eV/Å to avoid unreasonable atomic displacement during the structure optimization process. The stress convergence criterion was limited to within 0.05 GPa to ensure the mechanical stability of the crystal structure. Meanwhile, the maximum atomic displacement threshold was set to 10^{-3} Å to ensure the accuracy of the optimized structure configuration on a spatial scale. The calculation formula for the formation energy of oxygen vacancies on CaO and doped CaO surfaces is as follows.

$$E_{vac} = E(reduced) + 1/2E(O_2) - E(stoichiometric) \quad (3)$$

where $E(reduced)$, $1/2E(O_2)$, and $E(stoichiometric)$ represent the energy of the surface containing oxygen vacancies, the energy of oxygen atoms in O_2, and the energy of the complete surface, respectively. To compare the diffusion rate of O^{2-} and the desorption energy barriers of CO_2, the linear synchronous transit (LST) and quadratic synchronous transit (QST) methods [34,35] are employed, as presented in Equation (4).

$$E_a = E_{TS} - E_{IS} \quad (4)$$

where E_a is the activation energy barrier, and E_{TS} and E_{IS} are the diffusion energy and initial state energy, respectively. Adsorption energy (E_{ad}) is a key parameter for characterizing the strength of the interaction between the sorbent and the sorbate. Its numerical value directly reflects the thermodynamic driving force of the adsorption process. In this research system, E_{ad} is quantified using a specific calculation equation as follows:

$$E_{ad} = E_{CO_2+surface} - E_{CO_2} - E_{surface} \quad (5)$$

where $E_{CO2+surface}$ represents the total energy of the system after the CO_2 molecule binds to the sorbent surface, while E_{CO2} and $E_{surface}$ represent the independent energies of the CO_2 molecule and the sorbent surface, respectively. In addition, to further investigate the electronic interaction mechanism between the doped atoms and the calcium-based material surface, the partial density of states (PDOS) of the atoms in the system was calculated using the OptaDOS program [36].

3. Results and Discussion

In this study, a supercell CaO was developed. Following geometric optimization, the lattice constants became isotropic, with $a = b = c = 0.482$ nm, and the unit cell angles were $\alpha = \beta = \gamma = 90°$. This match confirmed the model's reliability. Given the limited relative fluctuation range of adsorption energy and the small total number of atoms in the system, after balancing the computational accuracy and efficiency, the model method constructed in Reference [16] was ultimately selected, with a five-layer CaO (001) surface model as the study system. Geometric structure optimization of CaO, Mg-CaO, Ni-CaO, and Mg–Ni-CaO models was performed using DFT calculations. After structural relaxation iteration calculations, stable configurations were obtained for each system. The specific structural characteristics and optimized structural parameters are shown in Figure 1 and Table 1. Structural analysis data show that in a pure CaO system, the bond lengths between Ca atoms and O-1 and O-2 atoms are 2.41 and 2.40 Å, respectively. However, when dopant

atoms are introduced, the crystal structure undergoes significant changes: in the Mg-CaO system, the distances between Mg atoms and O-1 and O-2 atoms are reduced to 2.30 and 2.13 Å, respectively; in the Ni-CaO system, the distances between Ni atoms and O-1 and O-2 atoms are 2.27 and 2.37 Å, respectively; and in the Mg–Ni-CaO synergistic doping system, the distance between Ni atoms and O-1 and O-2 atoms further decreased to 1.98 and 2.13 Å, respectively, while the distances between Mg atoms and O-1 and O-3 atoms were 2.31 and 2.15 Å, respectively. These data indicate that the introduction of doped atoms significantly changes the local atomic arrangement of CaO crystals and that the changes in atomic spacing may be closely related to the ionic radius and electronegativity differences of the doped atoms and their interactions with the CaO lattice.

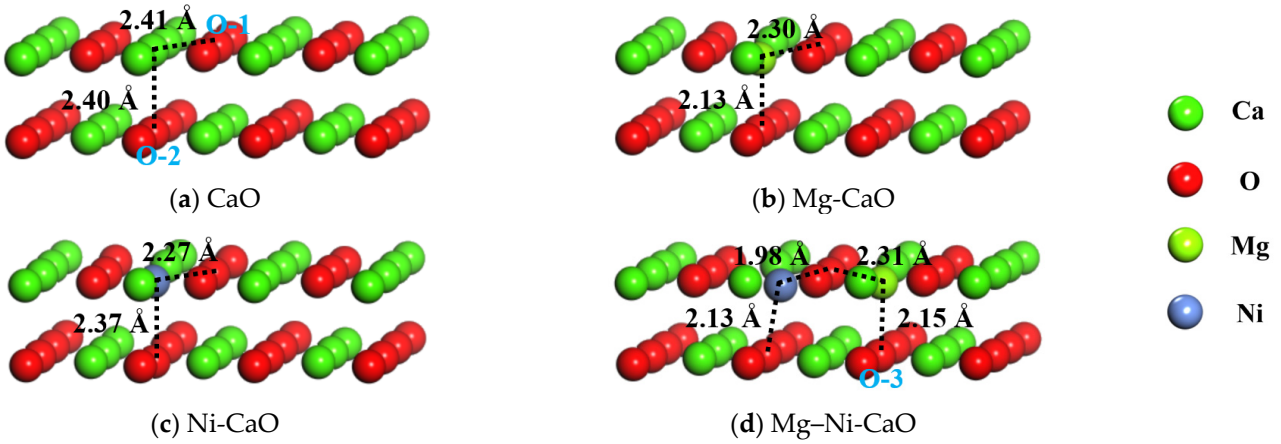


Figure 1. The view of CaO, Mg-CaO, Ni-CaO, and Mg–Ni-CaO.

Table 1. Interatomic distances between Mg, Ni, and O atoms in different doping systems.

Structure	Atomic Pair	Distance (Å)	Atomic Pair	Distance (Å)
CaO	Ca-O1	2.41	Ca-O2	2.40
Mg-CaO	Mg-O1	2.30	Mg-O2	2.13
Ni-CaO	Ni-O1	2.27	Ni-O2	2.37
Mg–Ni-CaO	Ni-O1	1.98	Ni-O2	2.13
	Mg-O1	2.31	Mg-O3	2.15

To investigate the effects of Mg doping, Ni doping, and Mg–Ni co-doping on the electronic structure of the CaO surface and to reveal their microscopic bonding mechanisms, Figure 2 presents the electron density plots for Mg-CaO, Ni-CaO, and Mg–Ni-CaO. These visualizations facilitate the quantitative analysis of their electronic structures. The results show that in Mg-CaO, Ni-CaO, and Mg–Ni-CaO, the doped Mg or Ni atoms exhibit stronger bonding with the surrounding O atoms due to enhanced electron overlap. This enhancement effect is reflected in the electron density map, where the Mg-O and Ni-O bond regions appear significantly redder, with red representing higher charge density. To better illustrate these interactions, we conducted PDOS analysis on Ni, Mg, and O atoms in Mg-CaO, Ni-CaO, and Mg–Ni-CaO, with the results presented in Figure 3. In Mg-CaO, the orbital hybridization peaks were found between Mg atoms and O-1 and O-2 atoms, indicating Mg-O covalent bond formation. Similarly, in Ni-CaO, peaks between Ni atoms and O-1 and O-2 atoms suggest Ni-O covalent bonds. In Mg–Ni-CaO, peaks between Mg atoms and Ni atoms, as well as O-1, O-2, and O-3 atoms, reveal Mg-O and Ni-O covalent bonds.

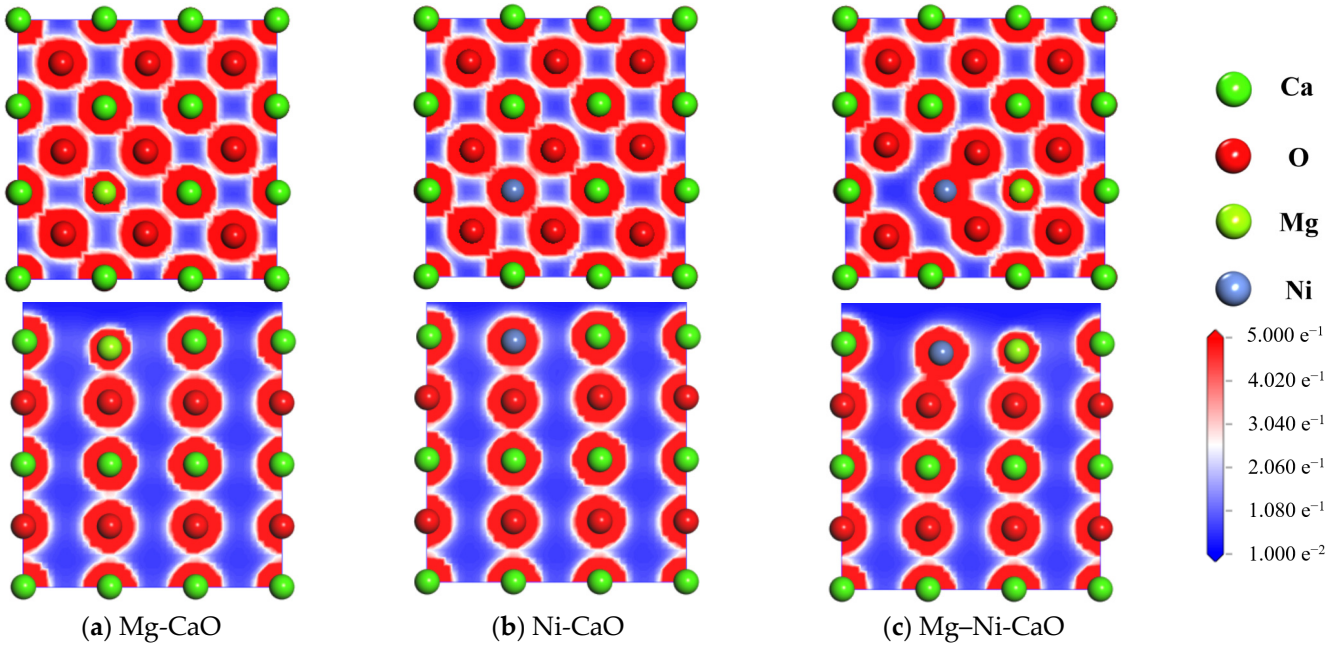


Figure 2. The density plots for Mg-CaO, Ni-CaO, and Mg–Ni-CaO.

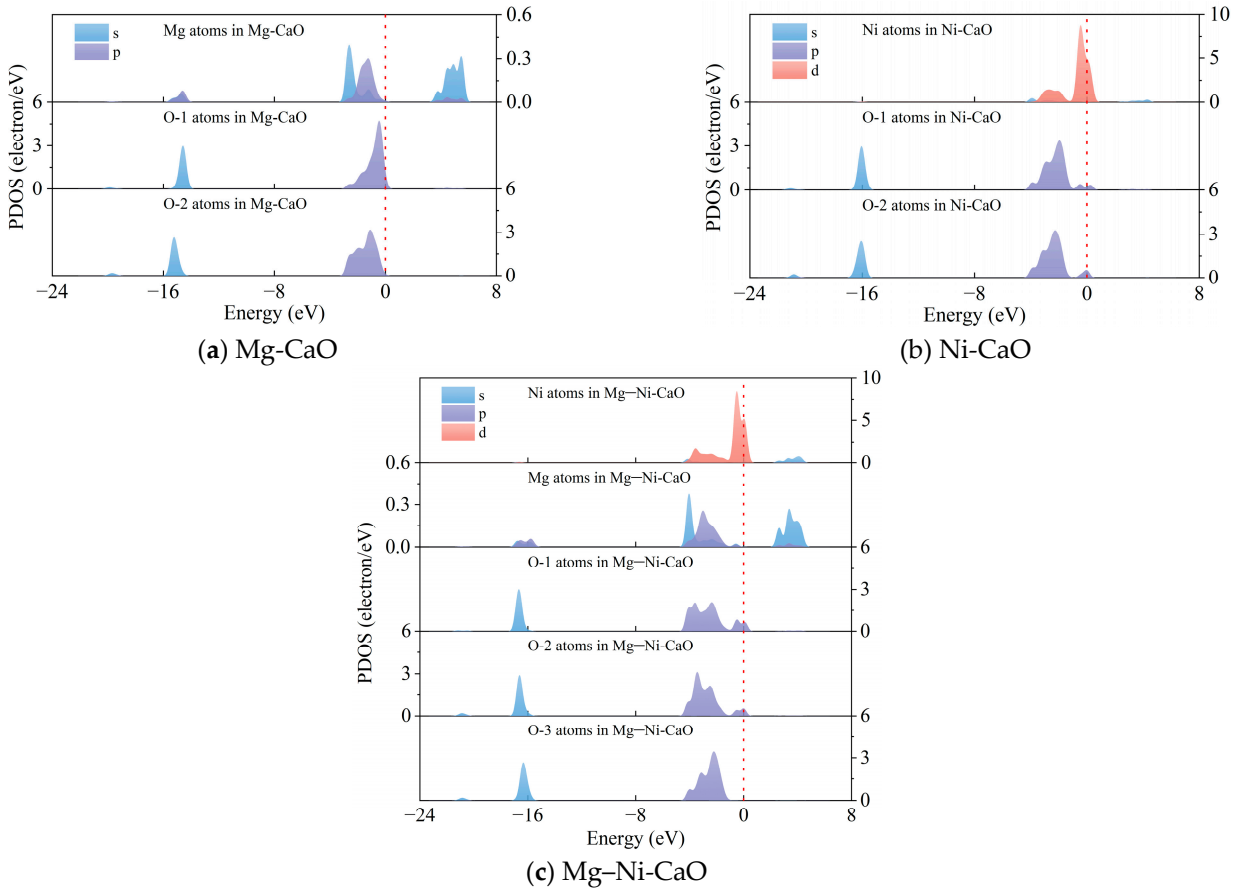


Figure 3. The PDOS diagrams in Mg-CaO, Ni-CaO, and Mg–Ni-CaO.

In calcium-based materials, oxygen vacancies can effectively create ion transport channels, thus greatly reducing the reaction activation energy. According to Equation (3), the oxygen vacancy formation energies for CaO, Mg-CaO, Ni-CaO, and Mg–Ni-CaO were calculated, as exhibited in Figure 4. It can be observed that the oxygen vacancy

formation energy in CaO is 6.842 eV, while those in Mg-CaO, Ni-CaO, and Mg–Ni-CaO are 6.625, 5.545, and 5.072 eV, respectively, all lower than CaO. Lower oxygen vacancy formation energy corresponds to a higher number of oxygen vacancies formed. The results indicate that both Ni and Mg single doping can effectively promote the formation of oxygen vacancies on the CaO surface. In the Mg–Ni co-doped system, the local lattice strain caused by Mg is coupled with the electronic effects of Ni, which leads to a redistribution of the charges around the doped atoms, further reducing the oxygen vacancy formation energy and making it easier for oxygen vacancies to form on the CaO surface.

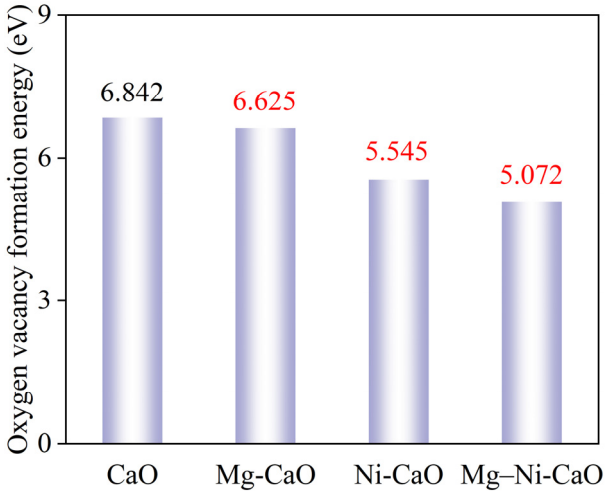


Figure 4. The oxygen vacancy formation energy of CaO, Mg-CaO, Ni-CaO, and Mg–Ni-CaO.

In the carbonization reaction system of calcium-based materials, the migration process of O^{2-} ions is the core link connecting material conversion and energy transfer, playing a decisive role in the thermodynamic equilibrium and kinetic process of the reaction. The diffusion rate of O^{2-} restricts the carbonation reaction. The energy barriers for O^{2-} diffusion on the surfaces of CaO, Mg-CaO, Ni-CaO, and Mg–Ni-CaO were calculated separately, according to Equation (4), as shown in Figure 5. The energy barrier for O^{2-} diffusion on the CaO surface is 4.606 eV. In contrast, on the Mg-CaO surface, it is 4.519 eV; on the Ni-CaO surface, it is 3.927 eV; and on the Mg–Ni-CaO surface, it is 2.692 eV. The energy barrier required for O^{2-} diffusion on the pure CaO surface is as high as 4.606 eV, reflecting the thermodynamic resistance to ion migration in the undoped system. However, after introducing dopant modification, the energy barrier shows a significant decreasing trend: on the Mg-CaO surface, the O^{2-} diffusion energy barrier decreases to 4.519 eV, with a relatively limited reduction; in the Ni-CaO system, this value further decreases to 3.927 eV, demonstrating the promotional effect of Ni doping on ion migration; notably, on the Mg–Ni-CaO co-doped surface, the O^{2-} diffusion energy barrier significantly decreases to 2.692 eV, which is notably lower than the single-doped system. The improved O^{2-} diffusion kinetics directly enhances the surface binding rates of O^{2-} and CO_2, which in turn greatly boosts the material's carbonation reaction activity.

Subsequently, in order to investigate the interaction between different material surfaces and CO_2, the optimized CO_2 molecules were placed on the surfaces of CaO, Mg-CaO, Ni-CaO, and Mg–Ni-CaO, with an initial position 3 Å away from the surface, and their adsorption properties were studied in detail. The optimized structural results are depicted in Figure 6, indicating that CO_2 forms a stable CO_3^{2-} structure through interaction with surface oxygen atoms on the surfaces of the four materials. The results show that on the pure CaO surface, the E_{ad} of CO_2 is −1.484 eV, while after Mg and Ni single doping modification, the E_{ad} values decrease to −1.522 eV and −1.627 eV, respectively, indicating

that the introduction of both elements can significantly improve the adsorption capacity of the material for CO_2. Notably, in the Mg–Ni co-doped system, the adsorption energy of CO_2 further decreased to −1.703 eV, directly confirming the synergistic doping effect of Mg and Ni. By regulating the electronic structure and distribution of active sites on the material's surface, the interaction between CO_2 molecules and the adsorbent surface can be more efficiently enhanced.

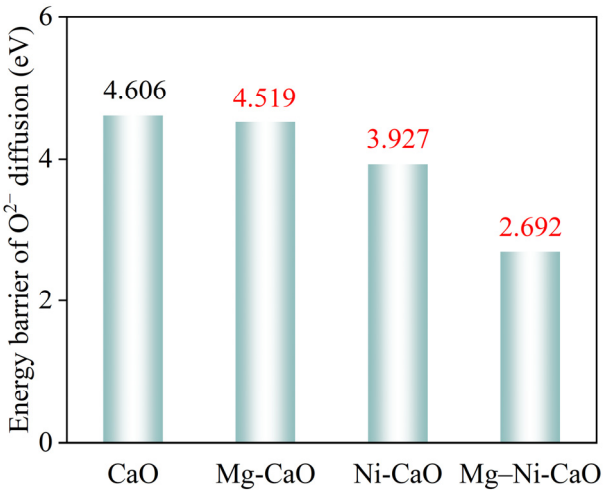


Figure 5. Energy barrier of O^{2-} diffusion for CaO, Mg-CaO, Ni-CaO and Mg–Ni-CaO.

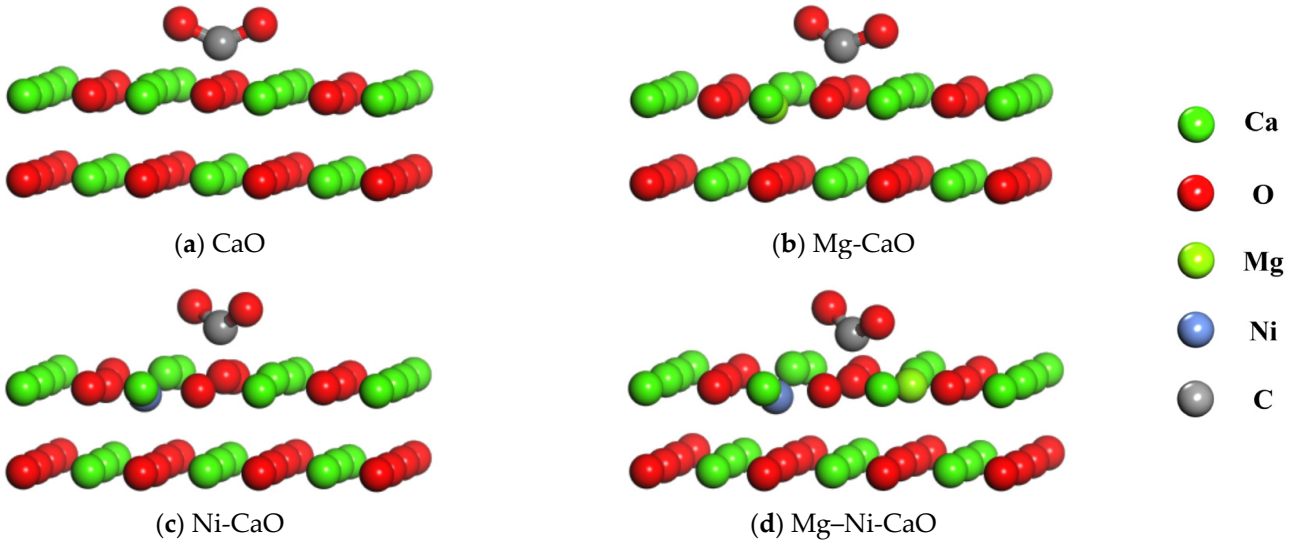


Figure 6. CO_2 adsorption optimization diagram.

To further reveal the interaction mechanism between O atoms on the CaO surface and C atoms in CO_2, PDOS analysis was performed on C and O atoms, and the results are shown in Figure 7. The results show that on the CaO surface, five significant resonance peaks occur between O atoms and CO_2's C atoms. These peaks are at −20.33, −18.75, −8.33, −6.62, and 4.50 eV. This means that the C atom and the O atom have a high degree of effective overlap between their orbitals, and the electron clouds interact strongly and reorganize. The surfaces of Mg-CaO, Ni-CaO, and Mg–Ni-CaO also exhibit the phenomenon of C and O atomic orbital hybridization and the formation of stable chemical bonds. Specifically, on the Mg-CaO surface, the resonance peaks between O atoms and CO_2's C atoms are at −20.75, −19.18, −8.70, −6.94, and 4.20 eV. On the Ni-CaO surface, these peaks are at −21.22, −19.24, −8.80, −6.78, and 4.20 eV. On the Mg–Ni-CaO surface, the peaks are at −21.28,

−19.38, −8.95, −6.92, and 4.15 eV. Notably, the resonance peaks on Mg- and Ni-doped CaO surfaces exhibit a downward energy shift. This indicates that Mg and Ni doping significantly enhance the interaction between C and O atoms. Moreover, with Mg–Ni co-doping, this shift is even more pronounced, further strengthening the C-O interaction. This electronic structure change aligns with the adsorption energy trend.

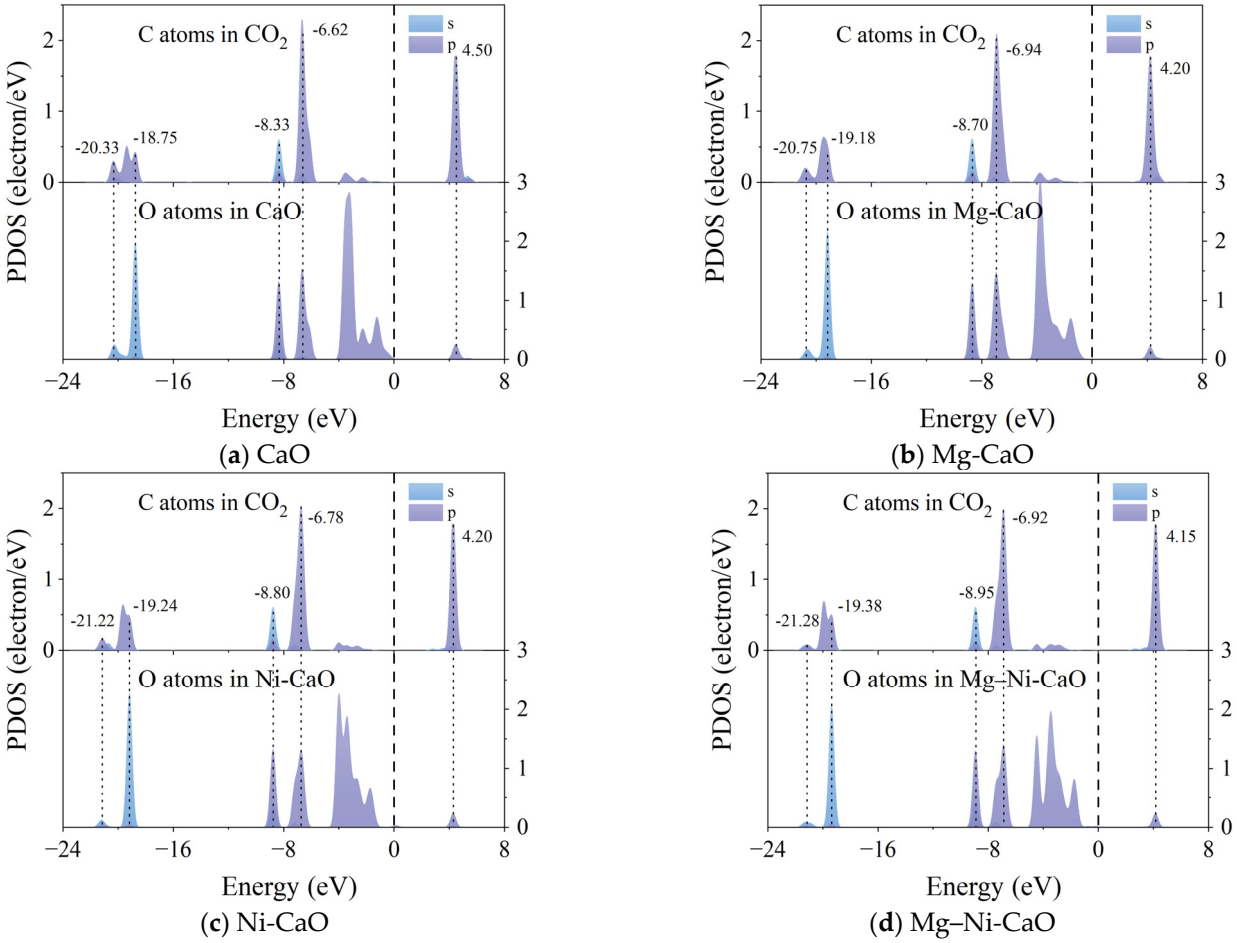
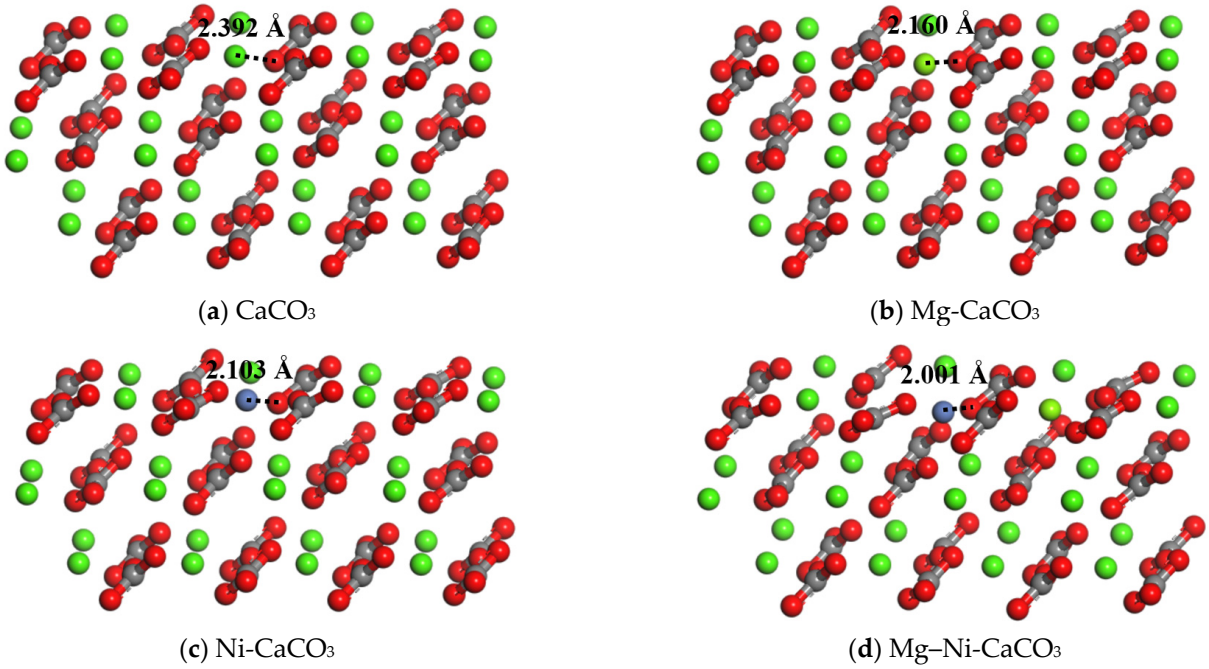


Figure 7. The PDOS diagrams in CaO, Mg-CaO, Ni-CaO, Mg–Ni-CaO, and CO_2.

In investigating the CO_2 desorption process, this study constructed the most thermodynamically stable $CaCO_3$ (104) crystal plane model based on reference [16]; see Figure 8. Through a detailed analysis of the individual CO_3^{2-} structures in the optimized model, it was found that the C-O bond lengths were 1.28, 1.31, and 1.32 Å, corresponding to bond populations of 0.89, 0.8, and 0.79, respectively. According to the chemical bond theory, bond length and bond density directly reflect bond stability. The chemical bond with a bond length of 1.32 Å and a bond density of only 0.79 is in a weaker bonding state and is more prone to breakage when energy is delivered. Based on this, this study selected this CO_3^{2-} structure as the core research object for the desorption process. Mg-doped, Ni-doped, and Mg–Ni co-doped $CaCO_3$ are shown in Figure 8b–d, respectively. The results indicate that the doping of Mg, Ni, and co-doping significantly changed the microstructural characteristics of the $CaCO_3$ surface. Specifically, in Mg-$CaCO_3$, the equilibrium distance between Mg atoms and O atoms in CO_3^{2-} is 2.160 Å. In Ni-$CaCO_3$, the distance between Ni atoms and O atoms in CO_3^{2-} is reduced to 2.103 Å; while in Mg–Ni-$CaCO_3$, the interaction distance between Ni atoms and O atoms in CO_3^{2-} is further reduced to 2.001 Å. This indicates that the doped elements can reconstruct the surface structure of $CaCO_3$ through coordination with CO_3^{2-}, and the synergistic effect of Mg and Ni atoms in the co-doped

system makes the interatomic interaction stronger, significantly shortening the distance between metal atoms and O atoms.



(**a**) $CaCO_3$ (**b**) Mg-$CaCO_3$

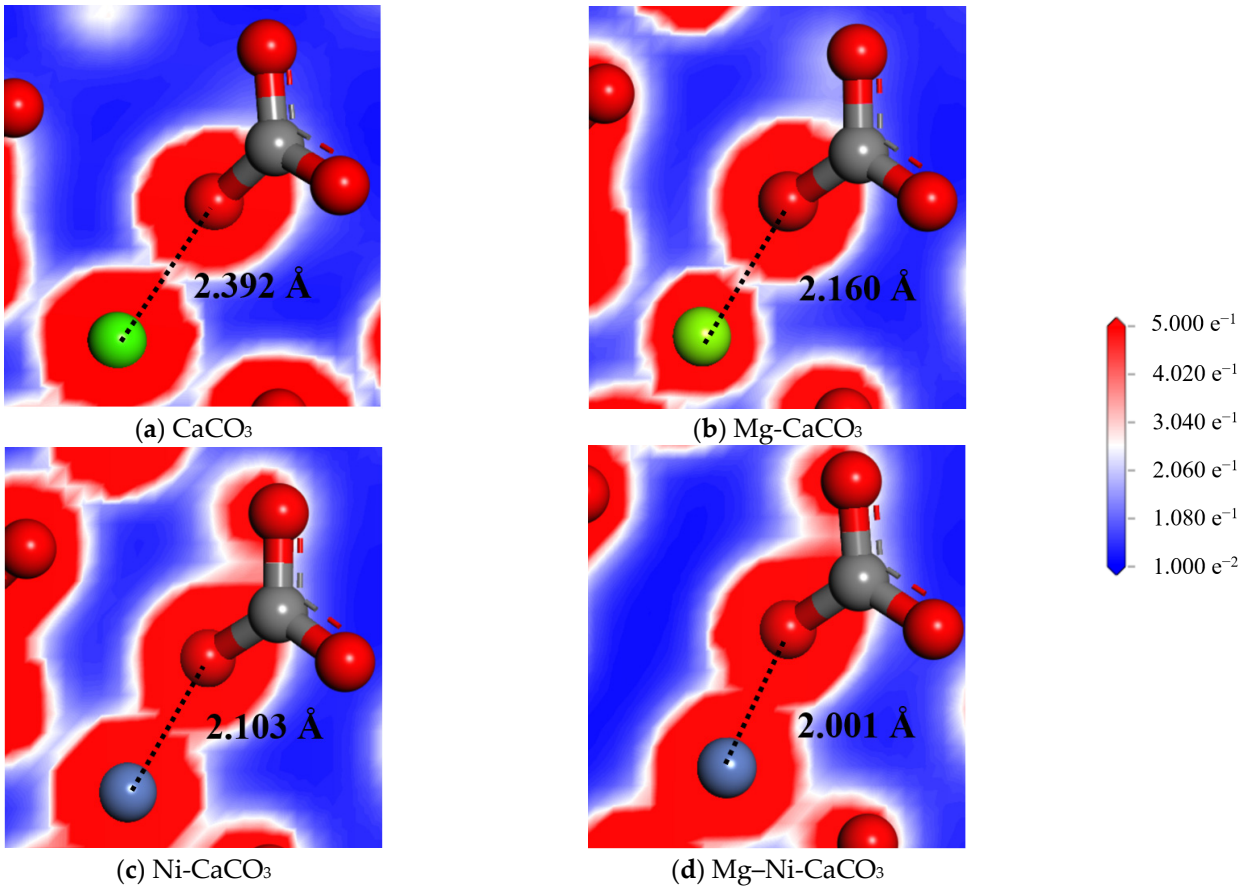
(**c**) Ni-$CaCO_3$ (**d**) Mg–Ni-$CaCO_3$

Figure 8. The view of $CaCO_3$, Mg-$CaCO_3$, Ni-$CaCO_3$, and Mg–Ni-$CaCO_3$.

To further reveal the interaction mechanism between the doped elements and the $CaCO_3$ surface, Figure 9 shows the electron density plot for $CaCO_3$, Mg-$CaCO_3$, Ni-$CaCO_3$, and Mg–Ni-$CaCO_3$. The analysis results indicate that in the $CaCO_3$ surface, the electron cloud distribution between Ca and O atoms is relatively independent, and there is no obvious charge overlap area, reflecting the weak interaction between them. In contrast, in Mg-$CaCO_3$, the electron clouds surrounding the Mg and O atoms show significant overlap, indicating that they form strong covalent bonds. Similarly, in Ni-$CaCO_3$ and Mg–Ni-$CaCO_3$, the electron clouds of Ni atoms and O atoms show significant overlap. In terms of reactivity, this strong interaction significantly alters the electron cloud distribution of the CO_3^{2-} ion, resulting in a reduction in the overlap of the C-O bond electron cloud on the doped surface and a significant weakening of the bond energy, thereby facilitating the release of CO_2.

Figure 10a illustrates the process of CO_2 desorption from $CaCO_3$. In the desorption reaction process on the $CaCO_3$ surface, the C-O chemical bond breaks first, accompanied by the reorganization of the electron cloud distribution, causing the O atom to remain at the active sites on the material surface. After the O atom is removed, the O-C-O structure gradually breaks free from the surface adsorption constraints under the combined effects of the system energy and steric hindrance, transitioning from the chemical adsorption state near the surface to the free gas phase state. Based on Equation (4), the CO_2 desorption energy barriers on the surfaces of $CaCO_3$, Mg-$CaCO_3$, Ni-$CaCO_3$, and Mg–Ni-$CaCO_3$ are obtained, as shown in Figure 10b. Specifically, on the $CaCO_3$ surface, CO_2 desorption requires overcoming an energy barrier of 4.850 eV. On the Mg-$CaCO_3$ surface, the energy barrier is 4.750 eV. When Ni is introduced for single doping, the energy barrier on the Ni-$CaCO_3$ surface is significantly reduced to 4.271 eV. Of note is that in the Mg–Ni-$CaCO_3$ co-doped system, the energy barrier required for CO_2 desorption further decreased to 3.922 eV. As can be seen, with the doping of Mg and Ni and their synergistic effects,

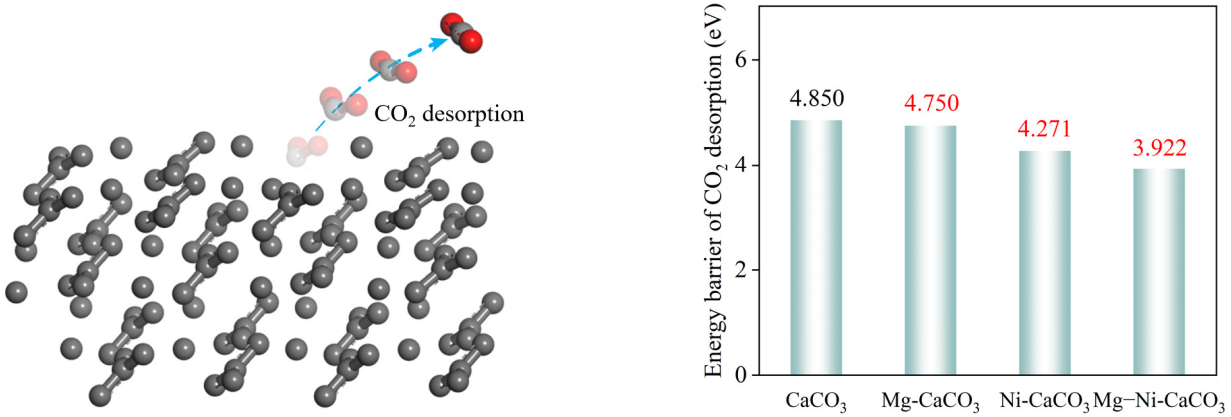
the CO_2 desorption energy barrier gradually decreases, significantly promoting the CO_2 desorption process.



(**a**) $CaCO_3$ (**b**) Mg-$CaCO_3$

(**c**) Ni-$CaCO_3$ (**d**) Mg–Ni-$CaCO_3$

Figure 9. The electron density plot for $CaCO_3$, Mg-$CaCO_3$, Ni-$CaCO_3$, and Mg–Ni-$CaCO_3$.



(**a**) CO_2 desorption diagrams (**b**) CO_2 desorption energy barriers

Figure 10. CO_2 desorption diagrams and CO_2 desorption energy barriers for $CaCO_3$, Mg-$CaCO_3$, Ni-$CaCO_3$, and Mg–Ni-$CaCO_3$.

4. Conclusions

This work uses DFT calculations to explore the effects of Ni and Mg doping on the CO_2 adsorption and desorption properties of calcium-based materials. The main results obtained are as follows:

(a) Both single doping and co-doping of Mg and Ni can significantly regulate the energy state of the CaO system. The oxygen vacancy formation energy for pure CaO is 6.842 eV, while for Mg-CaO, Ni-CaO, and Mg–Ni-CaO, it drops to 6.625 eV, 5.545 eV, and 5.072 eV, respectively. Mg–Ni co-doping exhibits stronger synergistic effects, further reducing the formation energy of oxygen vacancies and making them easier to form. During O^{2-} diffusion, the energy barrier on a pure CaO surface is 4.606 eV. On the surfaces of the Mg-CaO, Ni-CaO, and Mg–Ni-CaO doped systems, the O^{2-} diffusion energy barriers show significant differences, with values of 4.519, 3.927, and 2.692 eV, respectively. The synergistic doping of Mg and Ni can significantly reduce the energy threshold for ion migration, significantly enhancing O^{2-} diffusion efficiency and providing a more favorable ion transport pathway for CO_2 adsorption.

(b) Doping with Mg and Ni improved the adsorption capacity of CaO for CO_2. On the surfaces of CaO, Mg-CaO, Ni-CaO, and Mg–Ni-CaO, CO_2 forms stable CO_3^{2-} structures with surface O atoms, with adsorption energies of −1.484 eV, −1.522 eV, −1.627 eV, and −1.703 eV, respectively. Mg–Ni-CaO exhibits the highest CO_2 adsorption energy, indicating that it has the strongest adsorption capacity for CO_2. The PDOS analysis further revealed the microscopic mechanism of Mg and Ni doping enhancing CO_2 adsorption capacity. Namely, Mg and Ni doping shifted the energy of the resonance peak downward, and the energy shift was more obvious with co-doping, significantly enhancing the interaction between C and O atoms.

(c) The doping of Mg and Ni promotes the desorption process of CO_2. On the surfaces of $CaCO_3$, Mg-$CaCO_3$, Ni-$CaCO_3$, and Mg–Ni-$CaCO_3$, the energy barriers for CO_2 desorption are 4.850 eV, 4.750 eV, 4.271 eV, and 3.922 eV, respectively. The doping of Mg and Ni and their synergistic effect significantly reduced the CO_2 desorption energy barrier, greatly promoting the CO_2 desorption process.

Author Contributions: Conceptualization, W.S. and R.L.; methodology, R.L. and H.Y.; software, D.K.; validation, W.S., R.L. and D.K.; formal analysis, W.S. and H.Y.; investigation, D.K.; resources, X.B.; data curation, W.S. and X.B.; writing—original draft preparation, W.S.; writing—review and editing, D.K.; visualization, R.L. and D.K.; supervision, X.B. and H.Y.; project administration, X.B.; funding acquisition, X.B. All authors have read and agreed to the published version of the manuscript.

Funding: This study was supported by the Development of Science and Technology of Jilin Province, grant number YDZJ202301ZYTS254.

Data Availability Statement: Data are contained within the article.

Conflicts of Interest: The authors declare no conflicts of interest.

References

1. Zhao, C.; Ju, S.; Xue, Y.; Ren, T.; Ji, Y.; Chen, X. China's energy transitions for carbon neutrality: Challenges and opportunities. *Carbon Neutrality* **2022**, *1*, 7. [CrossRef]
2. Tian, X.; Guo, S.; Lv, X.; Lin, S.; Zhao, C.-Y. Progress in multiscale research on calcium-looping for thermochemical energy storage: From materials to systems. *Prog. Energy Combust. Sci.* **2025**, *106*, 101194. [CrossRef]
3. Wu, H.; Luo, C.; Luo, T.; Zhang, L.; Zhang, X.; Wu, F. Review of Solar Thermochemical Heat Storage Equipment and Systems Based on Calcium-Looping. *J. Energy Storage* **2024**, *103*, 114146. [CrossRef]
4. Lu, Y.; Xuan, Y.; Teng, L.; Liu, J.; Wang, B. A cascaded thermochemical energy storage system enabling performance enhancement of concentrated solar power plants. *Energy* **2024**, *288*, 129749. [CrossRef]
5. Jose, M.V. The Ca-looping process for CO_2 capture and energy storage: Role of nanoparticle technology. *J. Nanopart. Res.* **2018**, *20*, 39.
6. Ortiz, C.; Romano, M.C.; Valverde, J.M.; Binotti, M.; Chacartegui, R. Process integration of Calcium-Looping thermochemical energy storage system in concentrating solar power plants. *Energy* **2018**, *155*, 535–551. [CrossRef]
7. Alami, A.H.; Hawili, A.A.; Hassan, R.; Al-Hemyari, M.; Aokal, K. Experimental study of carbon dioxide as working fluid in a closed-loop compressed gas energy storage system. *Renew. Energy* **2019**, *134*, 603–611. [CrossRef]

8. Ramos, J.P.; Fernandes, C.M.; Stora, T.; Senos, A.M.R. Sintering kinetics of nanometric calcium oxide in vacuum atmosphere. *Ceram. Int.* **2015**, *41*, 8093–8099. [CrossRef]
9. Benitez-Guerrero, M.; Valverde, J.M.; Sanchez-Jimenez, P.E.; Perejon, A.; Perez-Maqueda, L.A. Multicycle activity of natural $CaCO_3$ minerals for thermochemical energy storage in Concentrated Solar Power plants. *Sol. Energy* **2017**, *153*, 188–199. [CrossRef]
10. Tian, X.K.; Lin, S.C.; Yan, J.; Zhao, C.Y. Sintering mechanism of calcium oxide/calcium carbonate during thermochemical heat storage process. *Chem. Eng. J.* **2022**, *428*, 131229. [CrossRef]
11. Raganati, F.; Chirone, R.; Ammendola, P. Calcium-looping for thermochemical energy storage in concentrating solar power applications: Evaluation of the effect of acoustic perturbation on the fluidized bed carbonation. *Chem. Eng. J.* **2020**, *392*, 123658. [CrossRef]
12. Sun, J.; Liu, W.; Li, M.; Yang, X.; Wang, W.; Hu, Y.; Chen, H.; Li, X.; Xu, M. Mechanical Modification of Naturally Occurring Limestone for High-Temperature CO_2 Capture. *Energy Fuels* **2016**, *30*, 6597–6605. [CrossRef]
13. Sanchez-Jimenez, P.E.; Valverde, J.M.; Perejón, A.; De La Calle, A.; Medina, S.; Pérez-Maqueda, L.A. Influence of ball milling on CaO crystal growth during limestone and dolomite calcination: Effect on CO_2 capture at Calcium Looping conditions. *Cryst. Growth Des.* **2016**, *16*, 7025–7036. [CrossRef]
14. Feng, J.; Guo, H.; Wang, S.; Zhao, Y.; Ma, X. Fabrication of multi-shelled hollow Mg-modified $CaCO_3$ microspheres and their improved CO_2 adsorption performance. *Chem. Eng. J.* **2017**, *321*, 401–411. [CrossRef]
15. Wang, A.; Deshpande, N.; Fan, L.S. Steam Hydration of Calcium Oxide for Solid Sorbent Based CO_2 Capture: Effects of Sintering and Fluidized Bed Reactor Behavior. *Energy Fuels* **2014**, *29*, 321–330. [CrossRef]
16. Kong, D.; Zhang, Y.; Nie, B.; An, N.; Zhu, Z.; Chen, Q. CO_2 adsorption and desorption across the Fe-doped Ca-based composites in the presence of H_2O: A DFT approach. *Phys. B Condens. Matter* **2024**, *673*, 415483. [CrossRef]
17. Valverde, J.M.; Sanchez-Jimenez, P.E.; Perez-Maqueda, L.A. Role of precalcination and regeneration conditions on postcombustion CO_2 capture in the Ca-looping technology. *Appl. Energy* **2014**, *136*, 347–356. [CrossRef]
18. Valverde, J.M.; Sanchez-Jimenez, P.E.; Perez-Maqueda, L.A. Effect of Heat Pretreatment/Recarbonation in the Ca-Looping Process at Realistic Calcination Conditions. *Energy Fuels* **2014**, *28*, 4062–4067. [CrossRef]
19. Manovic, V.; Anthony, E.J. Thermal activation of CaO-based sorbent and self-reactivation during CO_2 capture looping cycles. *Environ. Sci. Technol.* **2008**, *42*, 4170–4174. [CrossRef]
20. Sun, H.; Li, Y.; Bian, Z.; Yan, X.; Wang, Z.; Liu, W. Thermochemical energy storage performances of Ca-based natural and waste materials under high pressure during $CaO/CaCO_3$ cycles. *Energy Convers. Manag.* **2019**, *197*, 111885. [CrossRef]
21. Sarrión, B.; Perejón, A.; Sánchez-Jiménez, P.E.; Amghar, N.; Chacartegui, R.; Valverde, J.M.; Pérez-Maqueda, L.A. Calcination under low CO_2 pressure enhances the calcium Looping performance of limestone for thermochemical energy storage. *Chem. Eng. J.* **2021**, *417*, 127922. [CrossRef]
22. Huang, L.; Zhang, Y.; Gao, W.; Harada, T.; Qin, Q.; Zheng, Q.; Hatton, T.A.; Wang, Q. Alkali Carbonate Molten Salt Coated Calcium Oxide with Highly Improved Carbon Dioxide Capture Capacity. *Energy Technol.* **2017**, *5*, 1328–1336. [CrossRef]
23. Xu, Y.; Donat, F.; Luo, C.; Chen, J.; Kierzkowska, A.; Naeem, M.A.; Zhang, L.; Müller, C.R. Investigation of K_2CO_3-modified CaO sorbents for CO_2 capture using in-situ X-ray diffraction. *Chem. Eng. J.* **2023**, *453*, 139913. [CrossRef]
24. Choi, D.; Park, A.; Park, Y. Effects of eutectic alkali chloride salts on the carbonation reaction of CaO-based composites for potential application to a thermochemical energy storage system. *Chem. Eng. J.* **2022**, *437*, 135481. [CrossRef]
25. González, B.; Blamey, J.; McBride-Wright, M.; Carter, N.; Dugwell, D.; Fennell, P.; Abanades, J.C. Calcium looping for CO_2 capture: Sorbent enhancement through doping. *Energy Procedia* **2011**, *4*, 402–409. [CrossRef]
26. Yuan, C.; Liu, X.; Wang, X.; Song, C.; Zheng, H.; Tian, C.; Gao, K.; Sun, N.; Jiang, Z.; Xuan, Y.; et al. Rapid and stable calcium-looping solar thermochemical energy storage via co-doping binary sulfate and Al-Mn-Fe oxides. *Green Energy Environ.* **2023**, *9*, 1290–1305. [CrossRef]
27. Kong, D.; Nie, B.; Zhang, Y.; Chen, Q.; An, N.; He, N.; Yao, L.; Zhai, Y. A comprehensive understanding of the role of sodium sulfate in calcium looping via in-situ experiments and DFT studies: Performance and mechanism. *Fuel* **2024**, *371*, 131968. [CrossRef]
28. Kong, D.; Nie, B.; Zhang, Y.; Chen, Q.; An, N.; He, N.; Yao, L.; Wang, Z. Influence of Na_2SO_4-NaCl-ZnO co-doping on the thermochemical energy storage in CaO looping. *Fuel* **2024**, *375*, 132650. [CrossRef]
29. Kong, D.; He, N.; Chen, Q.; Nie, B.; Zhang, Y.; An, N.; Yao, L.; Wang, Z. Enhancement of Thermochemical Energy Storage by Alkali Metal Chloride Salts-Doped Ca-Based Sorbents: A Combined DFT and Experimental Study. *Molecules* **2024**, *29*, 6058. [CrossRef] [PubMed]
30. Clark, S.J.; Segall, M.D.; Pickard, C.J.; Hasnip, P.J.; Probert, M.I.J.; Refson, K.; Payne, M.C. First principles methods using CASTEP: Zeitschrift für Kristallographie-Crystalline Materials. *Z. Für Krist.* **2005**, *220*, 567–570.
31. Perdew, J.P.; Yue, W. Accurate and simple density functional for the electronic exchange energy: Generalized gradient approximation. *Phys. Rev. B Condens. Matter* **1986**, *33*, 8800–8802. [CrossRef]

32. Perdew, J.P.; Chevary, J.A.; Vosko, S.H.; Jackson, K.A.; Pederson, M.R.; Singh, D.J.; Fiolhais, C. Atoms, molecules, solids, and surfaces: Applications of the generalized gradient approximation for exchange and correlation. *Phys. Rev. B Condens. Matter* **1992**, *46*, 6671–6687. [CrossRef] [PubMed]
33. Perdew, J.P.; Burke, K.; Ernzerhof, M. Generalized Gradient Approximation Made Simple. *Phys. Rev. Lett.* **1998**, *77*, 3865–3868. [CrossRef] [PubMed]
34. Henkelman, G.; Jónsson, H. Improved tangent estimate in the nudged elastic band method for finding minimum energy paths and saddle points. *J. Chem. Phys.* **2000**, *113*, 9978–9985. [CrossRef]
35. Halgren, T.A.; Lipscomb, W.N. The synchronous-transit method for determining reaction pathways and locating molecular transition states. *Chem. Phys. Lett.* **1977**, *49*, 225–232. [CrossRef]
36. Morris, A.J.; Nicholls, R.J.; Pickard, C.J.; Yates, J.R. OptaDOS: A tool for obtaining density of states, core-level and optical spectra from electronic structure codes. *Comput. Phys. Commun.* **2014**, *185*, 1477–1485. [CrossRef]

Disclaimer/Publisher's Note: The statements, opinions and data contained in all publications are solely those of the individual author(s) and contributor(s) and not of MDPI and/or the editor(s). MDPI and/or the editor(s) disclaim responsibility for any injury to people or property resulting from any ideas, methods, instructions or products referred to in the content.